Bioinspiration & Biomimetics

PAPER

CFD-based multi-objective controller optimization for soft robotic fish with muscle-like actuation

To cite this article: Andrew Hess *et al* 2020 *Bioinspir. Biomim.* **15** 035004

Bioinspiration & Biomimetics

PAPER

RECEIVED
11 September 2019

REVISED
17 December 2019

ACCEPTED FOR PUBLICATION
20 January 2020

PUBLISHED
5 March 2020

CFD-based multi-objective controller optimization for soft robotic fish with muscle-like actuation

Andrew Hess[1,2], Xiaobo Tan[3] and Tong Gao[1,2]

[1] Department of Mechanical Engineering, Michigan State University,East Lansing, MI 48824, United States of America
[2] Department of Computational Mathematics, Science and Engineering, Michigan State University,East Lansing, MI 48824, United States of America
[3] Department of Electrical and Computer Engineering, Michigan State University,East Lansing, MI 48824, United States of America

E-mail: gaotong@egr.msu.edu

Keywords: artificial muscle, CFD, optimization, control, robotic fish

Abstract

Soft robots take advantage of rich nonlinear dynamics and large degrees of freedom to perform actions often by novel means beyond the capability of conventional rigid robots. Nevertheless, there are considerable challenges in analysis, design, and optimization of soft robots due to their complex behaviors. This is especially true for soft robotic swimmers whose dynamics are determined by highly nonlinear fluid-structure interactions. We present a holistic computational framework that employs a multi-objective evolutionary method to optimize feedback controllers for maneuvers of a soft robotic fish under artificial muscle actuation. The resultant fluid-structure interactions are fully solved by using a novel fictitious domain/active strain method. In particular, we consider a two-dimensional elastic plate with finite thickness, subjected to active contractile strains on both sides of the body. Compared to the conventional approaches that require specifying the entire-body curvature variation, we demonstrate that imposing contractile active strains locally can produce various swimming gaits, such as forwarding swimming and turning, using far fewer control parameters. The parameters of a pair of proportional-integral-derivative (PID) controllers, used to control the amplitude and the bias of the active strains, respectively, are optimized for tracking a moving target involving different trajectories and Reynolds numbers, with three objectives, tracking error, cost of transport, and elastic strain energy. The resulting Pareto fronts of the multi-objective optimization problem reveal the correlation and trade-off among the objectives and offer key insight into the design and control of soft swimmers.

1. Introduction

There has been tremendous interest in the development and design of soft robots in recent years, owing to rapid advancement of technology in soft actuators, sensing, and additive manufacturing. Compared to the conventional 'rigid' robots, soft robots can take advantage of a large number of degrees of freedom to achieve versatile locomotion and dexterous manipulation as many biological organisms do. These abilities open up the possibility of soft robots that are smaller, lighter, and more efficient than their traditional counterparts [3, 14, 31, 32, 39]. While many promising examples of soft robots have appeared, including soft swimmers emulating rays [34], juvenile jellyfish [33], and eel larvae [9], most soft robots use pneumatic actuation or cable-driven actuation [39], which presents challenges in terms of system complexity, noise, and footprint, among other concerns. Liquid crystal elastomers (LCE), dielectric elastomer (DEA) [9], and shape memory alloy [18], offer the promise of compact, muscle-like actuation for soft robots. However, understanding of the interplay between soft body and such muscle-like actuation remains limited. In particular, a systematic design tool for soft robotic systems is lacking that accounts for model dynamics and multiple objectives of interest.

Taking a soft swimmer as an example, in this paper we present a novel study on multi-objective optimization of feedback controllers for soft robots based on high-fidelity CFD simulation that explicitly accounts for muscle-like biomimetic actuation. Simulation of soft swimmers is challenging due to the coupled fluid dynamics and soft body mechanics in the

inertial regime where fast swimming motion requires a significant amount of momentum exchange between the fluid and solid structures to overcome viscous drag force. Nevertheless, instead of fully resolving such nonlinear fluid/elastic-structure interactions (FESI), people often oversimplify the problem by solving a reduced fluid-solid coupling system in mathematical modeling and numerical simulations. For example, the majority of numerical studies of fish-like swimmers assume that the undulatory motion (or swimming gait) approximately follows a traveling-wave form which can be experimentally measured for a free-swimming biological fish [18, 24, 46]. Typically, one treats the fish body as deformable but prescribes the curvature of its backbone deformation to a certain traveling-wave form [16, 43]. While convenient, these studies may oversimplify the nonlinear FESI to be a (quasi) one-way coupling problem, and, in the meantime, introduce too many free parameters to define the body actuation, which adds significant complexities in designing control schemes later. More importantly, soft swimmers will not always follow a specific swimming gait, which only approximate the solitary swimming motion at a quasi-steady state. In reality, they can constantly switch between straight-swimming and turning motions with acceleration/deceleration, especially when coordinating with many other swimmers during schooling [17, 23, 35].

To model soft actuation materials, an alternative to prescribing the entire body deformation or curvature is to build micro-mechanical models that take into account the intrinsic muscle-like behaviors locally. Generally speaking, there are typically two different ways of modeling the so-called artificial muscles. One way is to decompose the total deformation of the material into two parts: elastic deformation caused by mechanical stress and active deformation/strain caused by other stimuli [8, 30, 44]. For example, deformation of hydrogel can be decomposed into the elastic part and the swelling part [8]; deformation of liquid crystal elastomer can also be decomposed into the elastic strain and the stimuli-induced strain. Another approach is the active stress method, where the total stress is decomposed into a mechanical part and an active part, both of which can induce deformation [41]. In many cases, the above two methods can be flexibly used in achieving arbitrary deformations. In fact they are mathematically identical, due to the fact that the active deformation introduced here is a first-order approximation of nonlinear elasticity, and is independent of mechanical stress. These two methods have been widely used in modeling active soft elastic structures in biological systems (e.g. cardiovascular mechanics) and synthetic active soft materials [1]. While these elasticity models provide much more flexible yet simple local actuation schemes, solving for the resultant nonlinear deformation is computationally expensive when coupled with another (nonlinear) flow solver. To address these challenges, we have recently implemented the active strain approach in a fictitious domain (FD) method, and demonstrated that the FD/active-strain method is capable of solving the fully-coupled FESI for an arbitrary shape subjected to distributed contractive active strains [30].

In this work, we develop a holistic computational framework for the design, control, and optimization of a soft robotic swimmer. With the aid of the high-fidelity FD/active-strain simulator, we implement feedback control strategies for the fully-coupled fluid/elasticity systems under actuation. Here we model the robotic fish as a 2D swimming elastic beam of a finite thickness, with contractive strains being imposed on two sides (with sharp decays in the thickness direction) periodically. When coupled with fluid flows, we demonstrate that the resultant undulatory free-swimming motions can be tuned by changing the active strain magnitude and frequency. Moreover, turning motions of the swimmer can be effectively accomplished by imposing asymmetric active strains on the two sides of the body. To achieve feedback control of the swimming motion, we couple the FD simulator with model-free proportional-integral-derivative (PID) control, which, arguably, is the most widely used feedback control scheme [38]. We seek optimal parameters of the PID controllers by using a genetic-algorithm-based multi-objective evolution method, U-NSGA-III [40], which produces a Pareto set of optimal solutions that clearly illustrate the tradeoffs among the objectives, with which the designer is able to make informed decisions.

To put the study in context, we consider a series of tasks where the soft swimmer tracks a moving target involving different trajectories and velocities, where a pair of PID controllers are used to adjust the amplitude and the bias of the active contractile strains imposed on the swimmer. The parameters of the PID controllers are optimized with three objectives: (1) tracking error, (2) cost of transport, and (3) the average elastic strain energy of the morphing body. In particular, the tracking error refers to the error between the swimmer position and the moving target position and is thus a metric on tracking performance, while the cost of transport represents a measure of locomotion efficiency. The elastic strain energy is also of importance because it is not only closely related to the required performance of the actuator, but also to the rate of fatigue failure to which soft materials can be prone. The optimization is repeated at several Reynolds numbers for cases with different velocities and trajectories of a moving target. The resulting Pareto fronts of the multi-objective optimization problem reveal the correlations and trade-offs among the objectives and offer key insight into the design and control of soft swimmers. For example, the tracking error shows strong inverse correlation with the elastic energy. As another example, the optimized proportional gain parameters are also inversely related to the tracking error. Finally, the controller parameters produced via the proposed multi-objective optimization method demonstrate

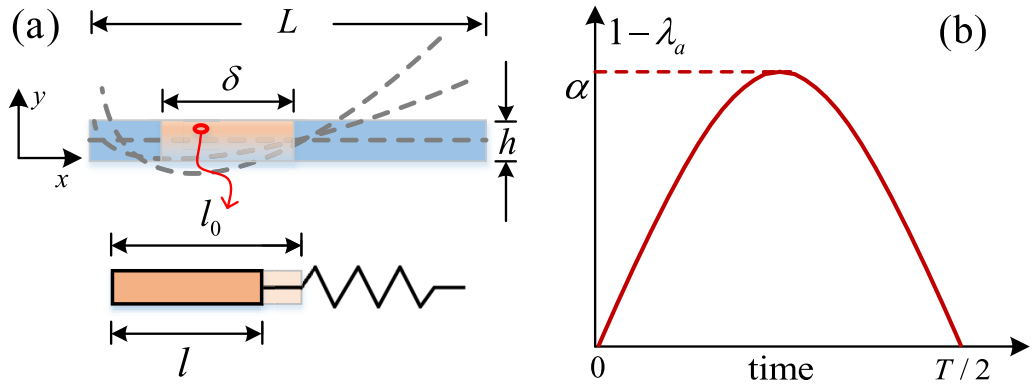

Figure 1. (a) Schematic of a 2D beam under contractile actuation (view from above). The active segment is of length δ. The microscopic mechanical model of the active contraction is illustrated by the zoom-in schematic on bottom. (b) Contractile actuation applied alternatively on the surfaces of two sides, which exponentially decays in the thickness (y) direction (not shown in the figure).

robustness across different conditions for the moving target and for the fluid environment.

The paper is organized as follows. In section 2 we briefly introduce the FD/active-strain method, and the computation model for the 2D soft robotic fish. In section 3 we integrate the CFD algorithm with a PID-based muscle control scheme, the parameters of which are optimized by using a higher-level multi-objective optimization algorithm. In section 4 we present numerical results and analyses on optimizing the PID controller parameters across a variety of swimming patterns, speeds, and Reynolds numbers. Finally conclusions and discussions are provided in section 5.

2. Review of FD/active-strain method

In this section, we briefly review the major components of the FD/active strain method, which is the core of our CFD solver. The reader is referred to [30] for more details, especially on the derivation of the FD formulation and the numerical schemes. Mathematically, the solid deformation can be described by the deformation gradient tensor $\mathbf{F} = \partial\mathbf{x}/\partial\mathbf{X}$, which projects the current deformed state to the initial reference state. To capture the local actuation, we decompose the deformation gradient tensor $\mathbf{F}$ into an active deformation tensor $\mathbf{F}_a$ and an elastic deformation tensor $\mathbf{F}_e$ following multiplicative decomposition [25, 26] such that

$$\mathbf{F} = \mathbf{F}_e \cdot \mathbf{F}_a. \tag{1}$$

Here $\mathbf{F}_a$ is effectively an arbitrary function applied to the reference configuration that can be designed in terms of the desired location, direction, sign and strength. For incompressible solids that are considered here, we apply an incompressible restriction on actuation such that $det(\mathbf{F}) = 1$, where 'det' represents the determinant. For simplicity, $\mathbf{F}_a$ can be defined in the principal coordinates and transformed to the desired orientation by a standard rigid body rotation coordinate transformation. For an artificial muscle that contracts uniaxially when activated, we define $\mathbf{F}_a = \text{diag}[\lambda_1, \lambda_2, \lambda_3]$, where $\lambda_1 < 1$ represents a principal compression ratio, and $\lambda_2 = \lambda_3 = \sqrt{\lambda_1^{-1}} > 1$ are correspondingly the homogeneous deformation in the other two directions. With the total $\mathbf{F}$ being mapped appropriately, the resultant elastic stress can be calculated through certain constitutive relation

$$\boldsymbol{\tau} = \boldsymbol{\tau}(\mathbf{F}_e) = \boldsymbol{\tau}\left(\mathbf{F} \cdot \mathbf{F}_a^{-1}\right) \tag{2}$$

for various kinds of material (hyperelastic, viscoelastic, composite, etc) conditions.

It is well understood that during an undulatory motion, fish use the anisotropic viscous drag force exerted in the longitudinal and transverse directions along the wavy body to create a net propulsive force [29]. As shown in figure 1(a), we adopt a simple 2D rectangular beam of length L and uniform thickness h to characterize the slender fish body shape. Without using complicated interconnected spring models to mimic the biological tissues' mechanical properties (e.g. the artificially coupled viscoelasticity and electrophysiology effects as what have been done by using the immersed boundary method [21, 45]), we assume that the soft active material is a continuous hyperelastic elastica which, at the microscopic level, is driven by a contracting element with an initial length l_0, yielding an effective local contraction ratio $\lambda_a = \frac{l}{l_0}$. At the microscopic scale, it connects with a neo-Hookean spring that generate elastic stresses in response to the active input of the contraction field. The latter, in 2D, is simply chosen as a homogeneous field $\mathbf{F}_a = \text{diag}\,(\lambda_a, \lambda_a^{-1})$ applied on the active segment.

Here we follow the geometry adopted by Hamlet *et al* [21] by choosing the first 10% of body length from the left to be passive, and then connecting an active section of length δ. To activate the beam, as shown in figure 1(b), we apply a constant ($\lambda_a \sim 1 - \alpha$, for a fixed α) or time-dependent (e.g. sinusoidal, $\lambda_a \sim 1 - \alpha \sin\left(\frac{2\pi}{T}t\right)$) contractile strain

field alternatively on both sides within a time period T. Here magnitude α characterizes the contraction strength. In the meantime, the maximum strain is imposed on the left (denoted by 'L') or right (denoted by 'R') side with an exponential decay in the thickness direction. Mathematically, it is convenient to define the sinusoidal actuation scheme as

$$\begin{cases} \lambda_a^L = 1 - \alpha \sin\left(\frac{2\pi t}{T}\right) \exp\left(-\frac{h-y}{d_0}\right), & t \in \left[0,\ \frac{T}{2}\right); \quad \lambda_a^L = 0, \quad t \in \left[\frac{T}{2}, T\right], \\ \lambda_a^R = 0, \quad t \in \left[0,\ \frac{T}{2}\right); \quad \lambda_a^R = 1 - \alpha \sin\left(\frac{2\pi t}{T}\right) \exp\left(-\frac{h-y}{d_0}\right), & t \in \left[\frac{T}{2}, T\right]. \end{cases} \tag{3}$$

In the above, d_0 controls the steepness of the decay, and is chosen as $h/3$ in all simulations in this work. Typical resultant bent shapes are illustrated in figure 1(a) by a few snapshots of the midline position (grey dashed lines). Therefore, continuously applying periodic contractions on both sides lead to an undulatory motion.

To resolve the FESI of soft robotic swimmers, we implement the above active strain model using a fictitious domain (FD) method [19, 30, 47]. The key idea of the FD method is that the interior of the solid is assumed to be filled with a fictitious fluid that is constrained to move at the same velocity with the solid by a pseudo body force (via a Lagrange multiplier). Mathematically, it is very similar to the immersed boundary method (IBM) [36] which typically employs overlaid Eulerian and Lagrangian meshes to solve the fluid-structure interactions: the Navier–Stokes (N-S) equations are solved on a fixed Eulerian mesh; while the embedded boundaries are tracked by a set of freely moving Lagrangian points.

Suppose that a deformable body of density ρ_s is immersed in the incompressible Newtonian fluid of viscosity μ and density ρ_f. Let Ω denote the entire computational domain containing both solid and fluid domains, and $S(t)$ represent the solid domain. It is noted that tracking swimming objects in the fixed coordinates requires using a very large computational domain, which makes computation expensive. Alternatively, here we employ an instantaneous inertial frame Ω that co-moves with the swimmer at a certain reference speed $\mathbf{U}$ [27]. Then the dimensionless FD governing equations in the weak form become

$$\int_\Omega \left(\frac{\partial \mathbf{u}_f}{\partial t} + \hat{\mathbf{u}}_f \cdot \nabla \mathbf{u}_f\right) \cdot \mathbf{v}_f \mathrm{d}\mathbf{x} + \int_\Omega \left(-p\mathbf{I} + \frac{1}{\mathrm{Re}}(\nabla \mathbf{u}_f)^T\right) : \nabla \mathbf{v}_f \mathrm{d}\mathbf{x} = \int_S \boldsymbol{\lambda} \cdot \mathbf{v}_f \, \mathrm{d}\mathbf{x}, \tag{4}$$

$$\int_\Omega q \nabla \cdot \mathbf{u}_f \mathrm{d}\mathbf{x} = \mathbf{0}, \tag{5}$$

where $\hat{\mathbf{u}}_f = \mathbf{u}_f - \mathbf{U}$. The dimensionless governing equations for neo-Hookean solid material ($\boldsymbol{\tau} = G(\mathbf{B} - \mathbf{I})$) are solved in the absolute references as

$$\begin{aligned} &\int_S \left[(\rho_r - 1)\left(\frac{d\mathbf{u}_s}{dt} - Fr\frac{\mathbf{g}}{g}\right)\right] \cdot \mathbf{v}_s d\mathbf{x} \\ &+ \int_S (\nabla \mathbf{v}_s)^T : [K_0 \ln J\mathbf{I} + G(\mathbf{B} - \mathbf{I})] d\mathbf{x} \\ &- \int_S (\nabla \mathbf{v}_s)^T : \left(-p\mathbf{I} + \frac{1}{\mathrm{Re}}[\nabla \mathbf{u}_f + (\nabla \mathbf{u}_f)^T]\right) d\mathbf{x} \\ &= -\int_S \boldsymbol{\lambda} \cdot \mathbf{v}_s d\mathbf{x}, \end{aligned} \tag{6}$$

$$\int_S (\mathbf{u}_f - \mathbf{u}_s) \cdot \boldsymbol{\zeta} d\mathbf{x} = \mathbf{0}. \tag{7}$$

Equations (4)–(7) represent the fluid momentum equation, the fluid continuity equation, the solid momentum equation, and the velocity constraint in the solid domain, respectively. In these equations, $\mathbf{u}_f$ is the fluid velocity, $\mathbf{u}_s$ the solid velocity, p the fluid pressure, and $\boldsymbol{\lambda}$ the pseudo body-force (i.e. the Lagrange multiplier). The variables $\mathbf{v}_f$, $\mathbf{v}_s$, q and $\boldsymbol{\zeta}$ are the corresponding variations, respectively. In our algorithm, we adopt a hybrid finite-difference/finite-element scheme [30] where the flow equations (4) and (5) are solved by the half-staggered finite difference scheme and the projection method [47], and the solid equation (6) is solved by using the finite element method (see details in [30]). Similar mixed schemes have also been implemented in the IBM solvers when handling various fluid-structure interaction applications [13, 20, 22].

For the original FD method for the passive deformation model, $\mathbf{B} = \mathbf{F} \cdot \mathbf{F}^T$ is the left Cauchy–Green deformation tensor, here $\mathbf{F}$ being the deformation gradient tensor defined as: $\mathbf{F} = \partial \mathbf{x}/\partial \mathbf{X}$, in which $\mathbf{x}$ and $\mathbf{X}$ are the current and reference configurations of the solid, respectively. J is the determinant of $\mathbf{F}$, and $J = 1$ for the incompressible solid. In contrast, for the active strain model studied, $\mathbf{B} = \mathbf{F}_e \cdot \mathbf{F}_e^T = (\mathbf{F} \cdot \mathbf{F}_a^{-1}) \cdot (\mathbf{F} \cdot \mathbf{F}_a^{-1})^T$, where $\mathbf{F}_e$ is the elastic deformation tensor which causes

the elastic stress, and $\mathbf{F}_a$ is an input deformation tensor without generating elastic stress. In addition, $\mathbf{g}$ denotes the gravitational acceleration. The following characteristic scales are used for the non-dimensionlization scheme: L_c for length, U_c for velocity, L_c/U_c for time, $\rho_f U_c^2$ for pressure p, and $\rho_f U_c^2/L_c$ for Lagrange multiplier $\boldsymbol{\lambda}$. The following dimensionless control parameters are also introduced: density ratio $\rho_r = \frac{\rho_s}{\rho_f}$, material parameters $K_0 = \frac{\overline{K}_0}{\rho_f U_c^2}$ and $G = \frac{\overline{G}}{\rho_f U_c^2}$, Reynolds number $\mathrm{Re} = \frac{\rho_f U_c L_c}{\mu}$, Froude number $Fr = \frac{gL_c}{U_c^2}$. Here $\overline{K}_0$ is related to the compressibility property of the material and $\overline{G}$ represents the shear modulus. It should be mentioned that for soft swimmers, the characteristic velocity is defined as $U_c = f_c L_c$ for a given reference actuation frequency f_c. In addition, in order to enforce the incompressibility constraint of the solid material, i.e. $J = 1$, we adopt a penalty function-like approximation by setting a large enough value for K_0 (10^4–10^5).

3. Controller design and optimization

3.1. Control scheme

The primary goal for our control scheme is to make the soft swimmer effectively follow a moving target point. Such situations could arise in applications such as schooling (i.e. leader-follower configuration) or simply following a pre-determined desired trajectory [4, 10, 28]. By its 2D nature our soft swimmer (elastic beam) is limited to forward swimming and turning, based on which we propose the following actuation scheme:

$$\alpha_R(t) = \alpha_0(t) + \frac{\beta(t)}{2}, \quad \alpha_L(t) = \alpha_0(t) - \frac{\beta(t)}{2}. \tag{8}$$

Here α_R and α_L correspond to the peak actuation strength in the right and left muscles, respectively, viewed in the body frame of the beam oriented from the tail toward the head. This differs from previous descriptions where both sides used a single value of constant α. It should be mentioned that as discussed below, their time-dependent values are determined via feedback control mechanisms. Here $\alpha_0(t)$ is the 'base' contraction strength for a forward (straight) swimming motion, which is assumed to be limited to the range $0 \leqslant \alpha_0 \leqslant \alpha_{max}$. After $\alpha_{R,L}(t)$ being computed in equation (8), we can compute the local contraction ratio $\lambda_a(t) = 1 - \alpha_{R,L}$, and then the active deformation tensor $\mathbf{F}_a(t) = \mathrm{diag}\,(\lambda_a, \lambda_a^{-1})$ (hence the elastic stress $\boldsymbol{\tau}$ in equation (2)).

Turning can be achieved by biasing the contraction strength between the two actuated sides. The soft swimmer tends to turn in the direction of the stronger actuation, providing a means to control the beam's heading while swimming. Testing showed that this mechanism allows the beam to turn even while it is at rest with an averaged swimming speed of zero. The bias that leads to turning is denoted by β and is limited to the range $-\beta_{max} \leqslant \beta \leqslant \beta_{max}$. Based on the signs in (8), a positive value of β causes the beam to turn to the right and vice versa. Note that α_R and α_L are limited to the same range as α_0 due to the physical constraints of the actuator, but the presence of β has the potential to push their values outside of this envelope. To prevent this while still achieving the desired bias, the portion of the bias outside the envelope is shifted to the opposite side. For example, if $\alpha_R = \alpha_0 + \frac{\beta}{2} \geqslant \alpha_{max}$, then $\alpha_R = \alpha_{max}$ and $\alpha_L = \alpha_{max} - \beta$. This is sufficient assuming that $\beta_{max} \leqslant \alpha_{max}$ and in practice we typically set $\beta_{max} = \frac{1}{2}\alpha_{max}$.

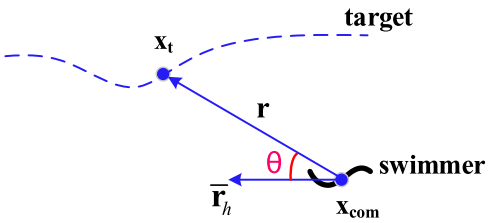

Figure 2. Schematic illustrating the control scheme based on the translational and rotational motion of a soft swimmer in relation to a moving target $\mathbf{x}_t$.

To complete the control scheme it is necessary to connect our control variables, α_0 and β, to the physical state of the swimmer. We elect to use proportional-integral-derivative (PID) controllers as they have been widely used across disciplines. A general PID controller takes the following form:

$$f(t) = k_p e(t) + k_i \int_0^t e(t')dt' + k_d \frac{de(t)}{dt} \tag{9}$$

where $f(t)$ is the control variable, $e(t)$ is the error corresponding to the difference between the target and current state, and the constants k_p, k_i, k_d are tuning parameters. The actuation strength $f(t) = \alpha_0(t)$ is calculated based on the error $e(t) = e_1(t)$ in position, which is defined as:

$$e_1(t) = |\mathbf{r}|\mathrm{sgn}\,(\mathbf{r} \cdot \mathbf{v})\,. \tag{10}$$

In the above, the vector $\mathbf{v}$ represents the moving target's velocity, and $\mathbf{r} = \mathbf{x}_t - \mathbf{x}_{com}$ connects the swimmer's center of mass (CoM) to the target position with its magnitude determining the magnitude of error (see schematic in figure 2). For stationary targets, i.e. $\mathbf{v} = 0$, we simply use $e_1(t) = |\mathbf{r}|$. On its own this error magnitude would lead to the error being always positive which can potentially promote overshoot and lead the integral term to blow up. To prevent this we determine the sign of the error by $\mathrm{sgn}(\mathbf{r} \cdot \mathbf{v})$ (here '$\cdot$' represents the vector inner product). If the target is moving away from the swimmer, $\mathbf{r} \cdot \mathbf{v}$ will be positive driving the swimmer to accelerate. Conversely, if the target is moving toward the swimmer, $\mathbf{r} \cdot \mathbf{v}$ will be negative causing the swimmer to slow down and potentially stop. If the controller returns a value that is out of bounds, the control variable is set to the respective bound and integration is stopped to prevent

windup of the integral term. The overall result is a follower type scheme where the swimmer tends to remain behind the target and overshoot behavior is suppressed.

Special attention must be given to the derivative term due to the noise in the error. This is a common problem in PID controllers as noise can produce large and drastically varying values of the derivative that can lead to undesirable behavior. The undulatory motion of the swimmer leads to a significant amount of sway which appears in the error as an oscillation driven at the forcing frequency. We filter out this oscillation by calculating the derivative based on the moving-average of the error, with the window size for averaging equal to that of the period of the forcing, T, as shown in (11). In particular, the following algorithm is used to approximate the derivative term:

$$\frac{de_1(t)}{dt} \approx \frac{\bar{e}_1(t) - \bar{e}_1(t-\Delta t)}{\Delta t}, \quad \bar{e}_1(t) = \frac{1}{T}\int_{t-T}^{t} e_1(t')dt'. \tag{11}$$

Directional control is achieved by determining $f(t) = \beta(t)$ via a separate PID controller, where the error $e(t) = e_2(t)$ is based on the angle between the target vector, $\mathbf{r}$, and the swimmer's time-averaged heading vector, $\bar{\mathbf{r}}_h$. Due to the highly flexible nature of the swimmer, it is difficult to clearly define a body frame. As such we choose to define our orientation in terms of a chord line running from the tail to the head of the swimmer, $\mathbf{r}_h$. The large-amplitude motion of the head and tail means that this vector will vary significantly across a full swimming stroke, limiting its value as an instantaneous measure. However, time-averaging like that done in (11) provides a stable measure of the swimmer's heading. In sum, the bias control is based on the error $e_2(t) = \theta$, the angle between the vectors $\mathbf{r}$ and $\bar{\mathbf{r}}_h = \frac{1}{T}\int_{t-T}^{t} \mathbf{r}_h(t')dt'$. Here $\mathbf{r}_h = \mathbf{x}_{head} - \mathbf{x}_{tail}$ represents the instantaneous direction vector that connects the head and tail. From the definition, since $\bar{\mathbf{r}}_h$ is already smoothed by the averaging, no special treatment is necessary for the derivative term.

3.2. Multi-objective optimization

Multi-objective optimization makes it possible to view the landscape of potentially optimal configurations. This allows for better understanding of the trade-offs between various objectives, leading to smarter design decisions. For example, in a swimmer a small decrease in speed may lead to sharp increase in efficiency or vice versa. The possibility of such a trade-off would not be apparent using single objective methods. The results of multi-objective optimization appear as a Pareto front, which is a surface in the objective space containing all solutions where each solution cannot be further improved in one objective without negatively affecting another objective(s).

Our work is focused on employing high-fidelity FSI simulations to investigate soft swimming mechanisms. This limits the use of reduced-order models, making evolutionary methods the most promising option for optimization. Locomotion traditionally lends itself to two major design objectives, swimming speed and efficiency. However, our fully coupled model allows us to consider other important design criteria such as those related to the actuation of the swimmer. Soft materials tend to have limited lifecycles and can experience premature fatigue failure compared to traditional actuators, if cyclic loading conditions are not accounted for. Thus the design of such soft swimmer robots may best be done with the consideration of 3 or more objectives.

We elect to optimize the soft swimmer by employing a multi-objective evolutionary method, specifically the U-NSGA-III method as developed by Seada and Deb [40]. NSGA-III [11] is a recent extension of the widely used NSGA-II [12] that incorporates the idea of predefined reference vectors, increasing the possible number of objectives from 2 to 3+. The weakness of NSGA-III is that this change also makes it ineffective in the case of 2 or fewer objectives, meaning it is not a replacement for NSGA-II but instead a complementary method. U-NSGA-III solves this problem by extending NSGA-III in such a way that one or two-objective optimization becomes possible, making it a well rounded method capable of any number of objectives.

The soft swimmer is driven by two PID controllers with three tuning parameters each, leading to a total of six parameters as summarized in Table 1. We optimize these parameters in terms of three objectives: combined average error ($\bar{e}$), cost of transport (C_{ot}), and average strain energy ($\bar{E}$), which are elaborated below.

The combined average error is the sum of the individually averaged errors as

$$\bar{e} = |\bar{e}_1| + |\bar{e}_2| \tag{12}$$

in which we track the entire evolution history during time t via $|\bar{e}_i| = \frac{1}{t}\int_0^t |e_i(t)|dt$, $i = 1, 2$. This provides a measure of tracking performance. The energy efficiency of the swimmer is evaluated through the measure of cost of transport,

$$C_{ot} = \frac{E_f}{d}, \tag{13}$$

where $E_f = \int_0^t P dt$ is the total energy imparted to the fluid calculated by integrating the imparted power P, and $d = \int_0^t |\overline{\langle \mathbf{u}(t') \rangle}| dt'$ is the path length determined from the averaged motion of the center of mass, in which we define $\overline{\langle \mathbf{u} \rangle} = \frac{1}{T}\int_{t-T}^{t} \langle \mathbf{u}(t') \rangle \, dt'$ and $\langle \mathbf{u} \rangle = \frac{1}{V}\int \mathbf{u} dV$ (here we calculate the integral for the solid velocity $\mathbf{u}$ in the Lagrangian domain of size V, and $\langle\rangle$ denotes a spatial average). Finally, the average total elastic strain energy is defined as

$$\bar{E} = \frac{1}{t}\int_0^t E(t')dt', \tag{14}$$

where we define $E = \int G(\mathrm{tr}(\mathbf{B}) - 2) \, dV$ for an incompressible neo-Hookean material [5]. This relates

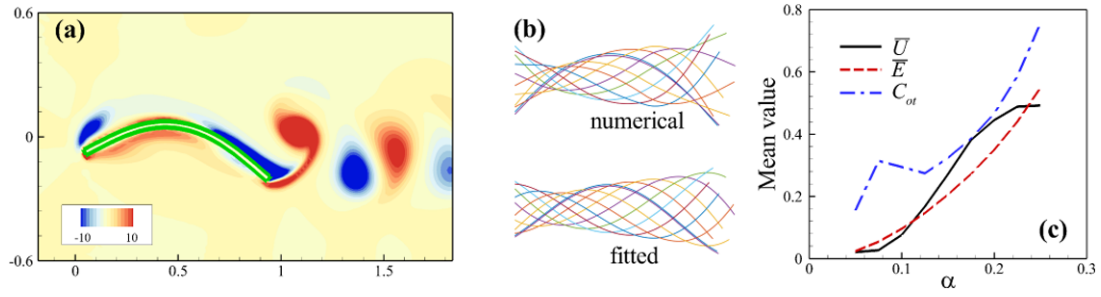

Figure 3. Free-swimming of a 2D elastic beam at Re = 500 and $T = 2.0$. (a) Instantaneous snapshot of vorticity field. (b) Envelope trajectories of the beam midline during one actuation period: (top) numerical results; (bottom) fitted results by equation (15). (c) Mean values of $\overline{U}$, $\overline{E}$, and C_{ot} as function of contraction strength α.

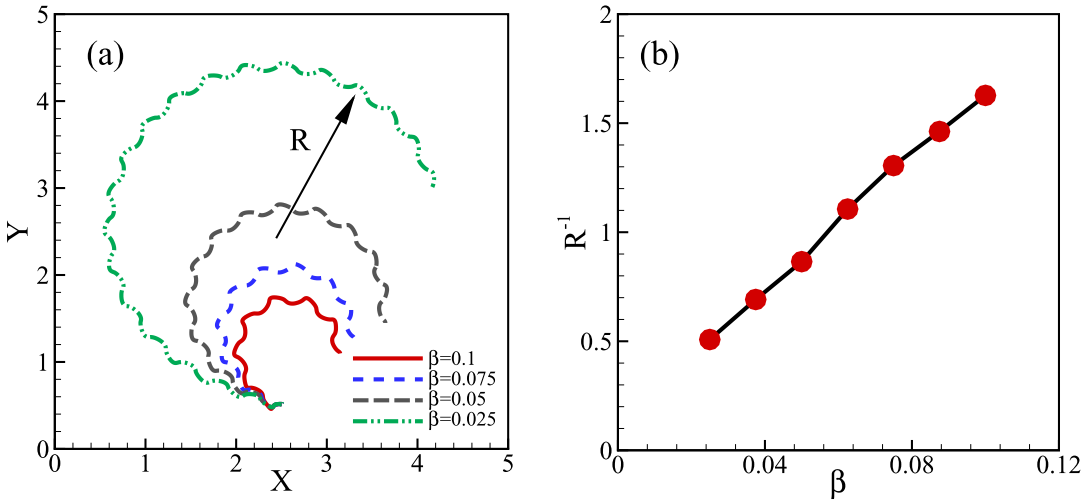

Figure 4. Simulation results for the soft swimmer at $\alpha_0 = 0.2$, Re = 500, and $G = 1000$: (a) center of mass (CoM) paths at different values of β; (b) Turning curvature R^{-1} as a function of β.

the force and energy requirements of the actuators as well as the potential for fatigue due to cyclic loading.

4. Results and discussion

4.1. Undulatory swimming

We have observed that after the initial transient, the soft swimmer quickly reaches a quasi-steady forward swimming with periodic undulatory body motion. In figure 3(a), we show a typical flow map of the swimmer when choosing Re = 500, $G = 1000$, $\delta = 0.4$, $T = 2$, and symmetric actuation at $\alpha = 0.15$ (namely, $\alpha_0 = 0.15$, $\beta = 0$ in equation (8)). A pair of vortices of opposite signs is generated during each tail upward/downward beating, leading to a reverse von Kármán vortex street. In figure 3(b), we show that the beam midline deformation extracted from the simulation during each time period (top), which can be approximately fitted by a weighted sine function (bottom):

$$\kappa(x,t) = (ax^2 + bx + c)\sin\left[2\pi\left(kx + \omega t\right) + \phi\right]. \tag{15}$$

In this case, we obtain the coefficients $a = -1.27$, $b = 0.92$, $c = 0.07$, $k = 0.4$, $\omega = 1.0$, and $\phi = 0.5$. Upon comparison, there is good match between the simulation result and the fitted model in the middle section while the front and tail sections show slight discrepancies. Overall, we see that our simple three-parameter (α_0, β, T) actuation scheme with muscle contraction is capable of reproducing various types of traveling-wave-like swimming gaits that typically require a larger parameter space.

For the forward swimming cases ($\beta = 0$), we have evaluated the mean values of swimming speed $\overline{U}$, elastic energy $\overline{E}$, and cost of transport C_{ot} as a function of the amplitude α_0 of muscle contraction when fixing Re = 500 and $T = 2$. As shown in figure 3(c), the system exhibits largely monotonic behaviors for the three examined variables when the actuation strength α is selected between 0.05 and 0.25, with an exception for C_{ot}, which shows a local peak around $\alpha = 0.08$. For very small values of α ($\alpha < 0.05$), the soft swimmer does not show significant directional motion; when $\alpha > 0.25$, we find that the average swimming speed (and hence also C_{ot}) decreases as α increases, suggesting that large body deformation does not necessarily lead to efficient swimming. In this study, we focus on the monotonic regime to facilitate controller design.

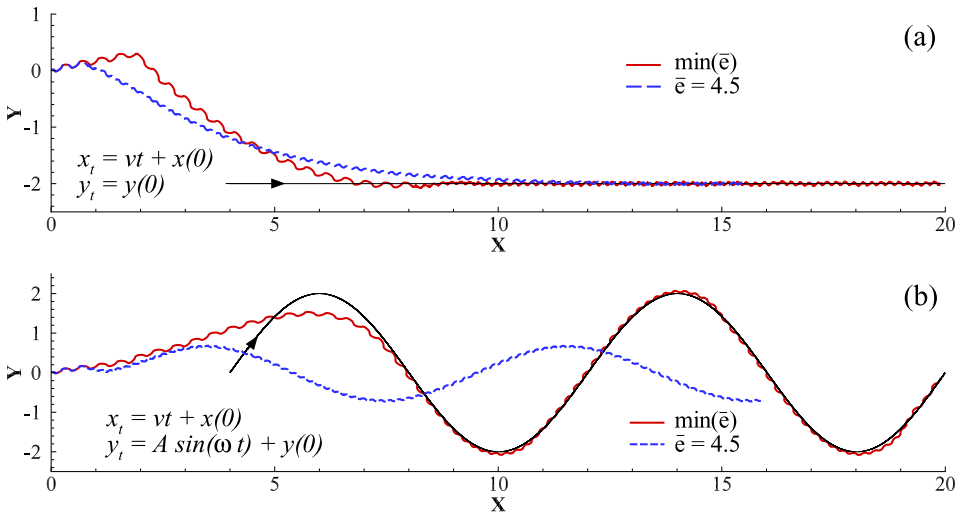

Figure 5. CoM trajectories of a soft swimmer tracking a moving target that is moving along both the (a) straight and (b) sinusoidal paths (black lines), when the swimmer is subjected to the PID control. The (red) and (blue) lines correspond to the controllers that have the lowest and a moderate error $\bar{e}$ (but lowest elastic energy $\bar{E}$), respectively. The black arrows mark the target's moving directions.

As discussed in section 1, specifying the empirical traveling-wave form of equation (15) only applies to the scenario of forward swimming. To achieve more elaborate maneuvering such as turning, we introduce a bias when applying contractions on the two sides of the swimming body. A similar turning study of a 2D eel-like swimmer was performed by Bhalla *et al* using the IBM solver [6]. Nevertheless, they have to specify the undulatory swimming motion on a curved body-axis. In figure 4, we demonstrate the effectiveness of the actuation scheme for turning with fixed actuation strength α_0 ($\alpha_0 = 0.2$) but increasing β. In figure 4(a), the swimmer's instantaneous CoM positions clearly show that it approximately follows a circular trajectory, the radius of which decreases (tighter turn) as the bias value β increases. Interestingly, the results in figure 4(b) suggest an almost linear relation between the bias value of β and the trajectory curvature R^{-1} (reciprocal of the radius).

4.2. Optimization and analysis

4.2.1. Trajectory comparison

To make sure the controller is effective, we optimize it by accounting for different scenarios of the moving target's characteristic velocity and the Reynolds number Re as defined at the end of section 2. Note that we define Reynolds number in terms of the actuation frequency, not a physical velocity, so by varying Re we are implying a change in the fluid properties, namely the viscosity. In these studies we employ two different types of target trajectories, a straight path as characterized in equation (16) and a sinusoidal path as expressed in equation (17). The swimmer starts from at rest facing along the x axis. We describe the straight trajectory of the target with a constant velocity v as

$$\mathbf{x}_t = \begin{cases} x_t = vt + x(0) \\ y_t = y(0) \end{cases}. \tag{16}$$

For the sinusoidal trajectory, the moving target has a constant velocity in the x direction, while its y position follows a sinusoidal function of time:

$$\mathbf{x}_t = \begin{cases} x_t = vt + x(0) \\ y_t = A\sin\omega t + y(0) \end{cases}. \tag{17}$$

Here we fix the amplitude, $A = 2$, and angular frequency, $\omega = 0.05\pi$. The inclusion of sinusoidal motion means that the swimmer has to constantly adjust its velocity and direction, which demonstrates its ability to follow complex paths. All cases are run with a maximum (dimensionless) simulation time of $t = 80$, and as a precaution, the forward velocity controller is not activated until $t = 2$ and the heading controller is not activated until $t = 4$. Before these times, $\alpha_0 = \alpha_{max}$ and $\beta = 0$. The idea is to allow a smooth start and prevent potentially large values of β from negatively affecting the starting behavior of the swimmer, by first allowing it to achieve a significant forward velocity. However, testing has shown both restrictions to be unnecessary if β_{max} is sufficiently smaller than α_{max}.

In figure 5, we show the performance of a soft swimmer when subjected to different PID controllers by comparing its CoM trajectories with the specified straight (panel (a)) and sinusoidal (panel (b)) paths (black lines). Here we select two optimal solutions, corresponding to the case of lowest error $\bar{e}$ ($min(\bar{e})$) and the case of a moderate error ($\bar{e} = 4.5$) but lowest elastic energy ($min(\bar{E})$) at Re $= 500$. For the minimum error examples in both panels, the swimmer quickly converges to the target point's position and is able to follow it closely. Note that the target is a moving point

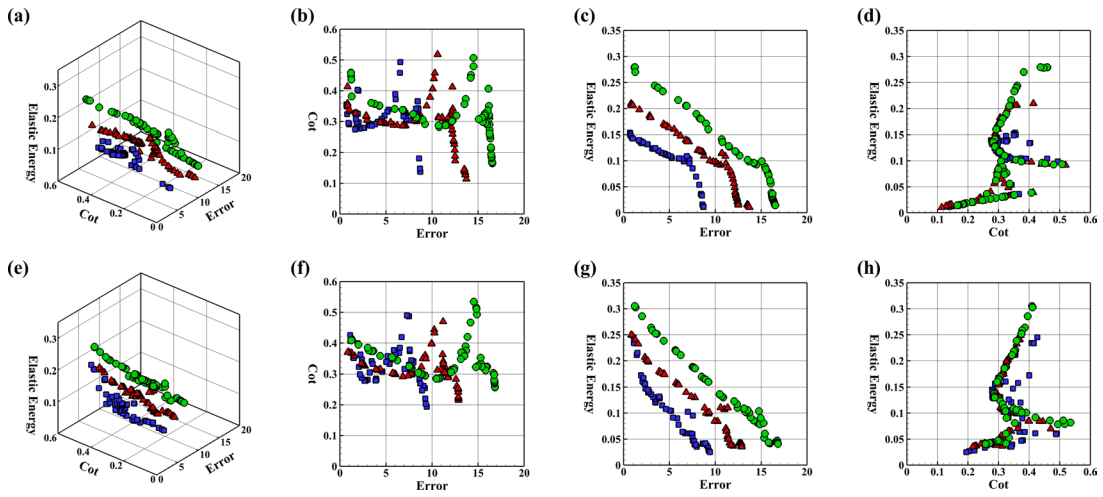

Figure 6. Pareto fronts in the space of tracking error ($\bar{e}$), cost of transport (C_{ot}), and elastic strain energy ($\bar{E}$) for various target speeds v with Re = 500. Blue-square: $v = 0.1$. Red-triangle: $v = 0.2$. Green-circle: $v = 0.3$. Straight path: (a)–(d). Sinusoidal path: (e)–(h). The leftmost panels (a) and (e) are 3D views of the objective spaces. The panels to their right are 2D projections of the respective distribution that visualize the trends between each pair of objectives. (b) and (f): $\bar{e}$ versus C_{ot}. (c) and (g): $\bar{e}$ versus $\bar{E}$. (d) and (h): C_{ot} versus $\bar{E}$.

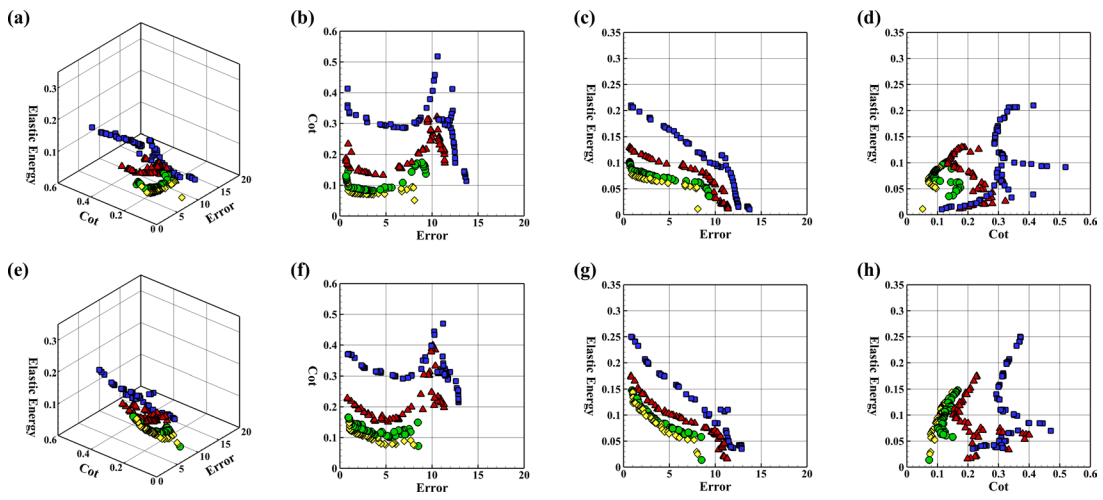

Figure 7. Pareto fronts in the space of tracking error ($\bar{e}$), cost of transport (C_{ot}), and elastic strain energy ($\bar{E}$) for various Re with $v = 0.2$. Blue-square: Re = 500. Red-triangle: Re = 1000. Green-circle: Re = 1500. Yellow-diamond: Re = 2000. Straight path: (a)–(d). Sinusoidal path: (e)–(h). The leftmost panels (a) and (e) are 3D views of the objective spaces. The panels to their right are 2D projections of the respective distribution that visualize the trends between each pair of objectives. (b) and (f): $\bar{e}$ versus C_{ot}. (c) and (g): $\bar{e}$ versus $\bar{E}$. (d) and (h): C_{ot} versus $\bar{E}$.

and not simply a designated path, meaning that a close match to the target trajectory implies the swimmer must be matching both the desired heading and velocity. Variation in the velocity can be discerned by observing the variation in the wavelength of the undulatory oscillations in the CoM trajectory. For a fixed driving frequency, the swimmer's velocity will correspond to the wavelength of this oscillation. At the start the wavelength is long as the swimmer attempts to reach the target as quickly as possible. The wavelength then shortens as the swimmer approaches the target and matches its velocity. In the sinusoidal case, the wavelength is shorter near the peaks and longer in between corresponding to the velocity of the sine function which varies by the cosine. In contrast, for the moderate error case, we see that the swimmer appears to lag behind, and eventually fails to catch up to the target, although the small amplitudes (relative to the best $\bar{e}$ cases) indicates lower contractile strengths which implies less deformation of the body and thus lower elastic strain energy.

4.2.2. Pareto fronts of optimized solutions

Here we show global views of the obtained optimal solutions. Figure 6 compares the resulting Pareto fronts (a set of nondominated optimal solutions if no objective can be improved without sacrificing at least one other objective) in the space of objectives when the target velocity v takes different values while the Reynolds number Re is kept at 500, for the cases of straight trajectory ((a)–(d)) and sinusoidal trajectory ((e)–(h)), respectively. The obtained optimal solutions

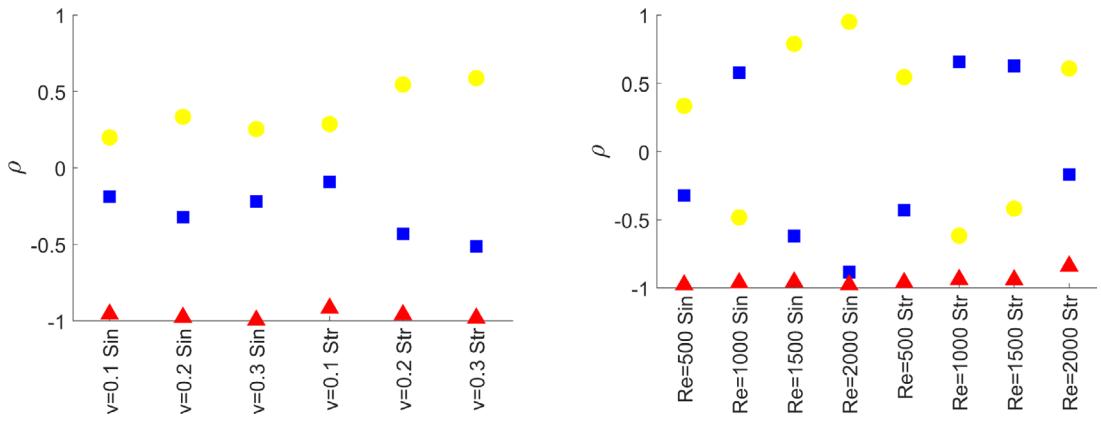

Figure 8. Comparison of the Pearson correlation coefficients (ρ) of the objectives for varying ν (left) and varying Re (right). Blue-square = $\bar{e}$ to C_{ot}. Red-triangle = $\bar{e}$ to $\bar{E}$. Yellow-circle = C_{ot} to $\bar{E}$.

for these two different paths are approximately allocated in the same regimes, exhibiting very similar patterns. Figure 7 shows the results when the Reynolds number is varied while the velocity is fixed at 0.2. All datasets shown correspond to a total of 50 generations of evolution with a child population of 64. The swimmer's body is neutrally buoyant with $\delta = 0.5$ and non-dimensional parameters $G = 1000$ and $K_0 = 10^4$. It is worthwhile to mention that some portions of the objective space, and the individual solutions (PID parameters) that fall within, may be undesirable. For example, there are scenarios when the swimmer is barely moving and possibly not swimming at all. This 'trivial' state can be interpreted using the three objectives, where the ideal optimal value of strain energy, $\bar{E} = 0$, coincides with the trivial case of zero actuation, $\alpha_R = \alpha_L = 0$. From the optimizer's prospective, this is a valid solution because our objective functions do not in any way represent this as a negative behavior. The objective functions could possibly be modified to avoid this trivial solution by adding a penalty function or cutoff, but such changes are undesirable since they could potentially add constraints or biases on the optimizer in unpredictable ways. Thus we stick to the original form of objective functions and remove trivial solutions in the end as part of the final decision-making process.

A 2D view of the Pareto front on the projected $(\bar{E}, \bar{e})$ plane can clearly reveal the effect of varying ν on the resulting optimal solutions, as seen in figures 6(c) and (g). The distributions are clearly separate with the profile shifting up and right as ν increases, both as expected, since increasing ν indicates the increase in tracking difficulty and the requirement of higher actuation output. In comparison, the effect on C_{ot} as seen in figures 6 (b), (d), (f) and (h) appears to be minimal with the profiles being nearly independent of ν.

Varying Re proves to have a significantly different effect with dependency apparent primarily in C_{ot} and $\bar{E}$ as can be seen in figure 7. From figures 7(b), (d), (f) and (h), we see that as Re increases, C_{ot} drops. From figures 7(c) and (g), the elastic strain energy also drops with increasing Re. As Re increases the viscous forces acting on the swimmer decrease, leading to both a lower C_{ot} and actuation strength required to drive the swimmer. In all cases, for the regions where the error $\bar{e}$ is low, there is an inverse relationship between C_{ot} and the error. The error proves to be mainly dominated by the positional error, e_1, which in turn is logically inversely related to the swimmer's velocity. From this we can conclude that C_{ot} increases with increasing swimmer velocity as expected due to fluid drag.

4.2.3. *Objective correlations and parameter trends*

In figure 8 we further compare the Pearson correlation coefficients of the objectives for each data set. The most apparent result is that in all cases the coefficient relating $\bar{e}$ and $\bar{E}$ is approximately equal to -1. This means that they are correlated strongly with an inversely proportional relationship, which is confirmed by observing panels (c) and (g) in figures 6 and 7 where the population in each dataset has a highly linear distribution. Physically this indicates that lower error requires stronger actuation. The strength of this correlation also implies that these objectives are not independent in our system. For example, it is not possible to find an optimal solution that decreases both $\bar{e}$ and $\bar{E}$ simultaneously.

The Pearson coefficients relating $\bar{e}$ to C_{ot} as well as relating C_{ot} to $\bar{E}$ do not show similarly clear patterns. Qualitatively, in the regions of lower $\bar{e}$ there appear to be noticeable and consistent trends; however, when viewed as a whole, these fall apart. Thus without defining a criterion to trim the data set, a solid conclusion cannot be made. Interestingly it can be noted that coefficients relating $\bar{e}$ to C_{ot} and those relating C_{ot} to $\bar{E}$ appear to be equal in magnitude and inverted in sign. This can be explained by the objectives in each dataset falling roughly in a plane such that the distribution seen in panels (b) and (f) (corresponding to $\bar{e}$ to C_{ot}) is the mirror of that seen in panels (d) and (h) (corresponding to C_{ot} to $\bar{E}$).

Furthermore, we seek more quantitative understandings of how the controller parameters vary when

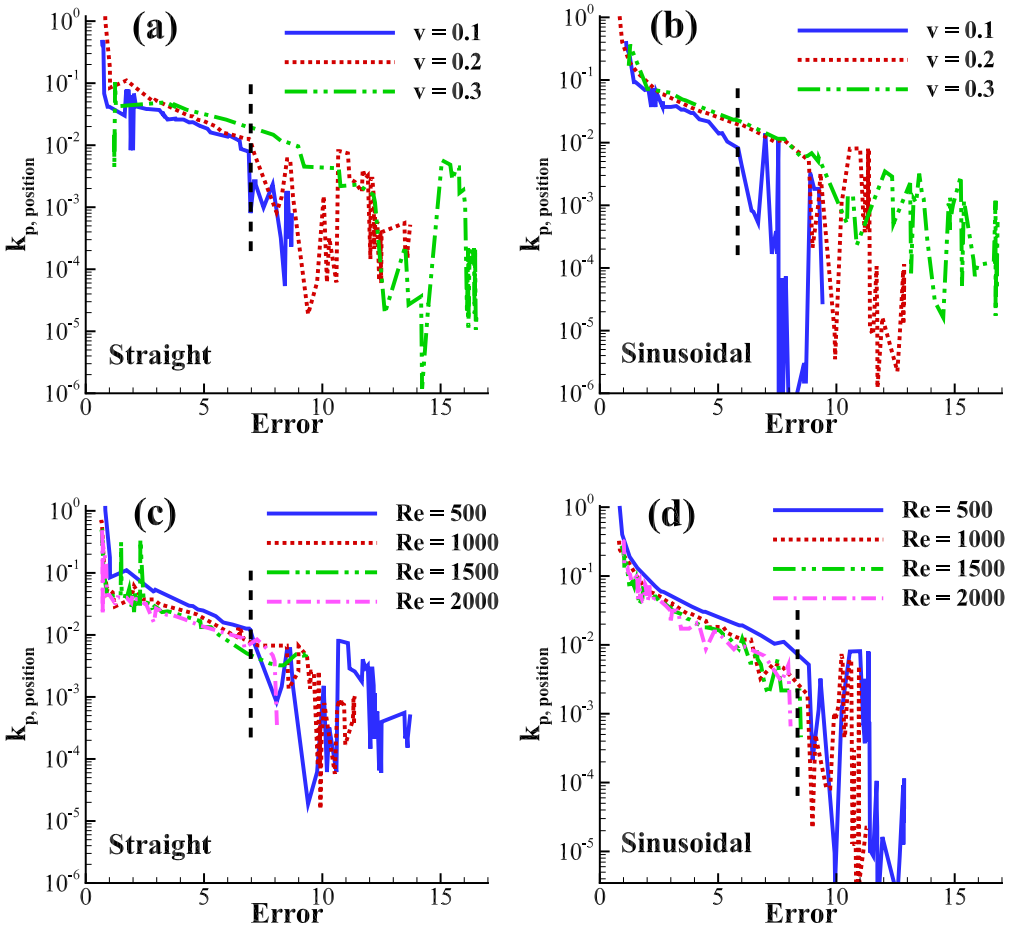

Figure 9. The trends of $k_{p,position}$ versus $\bar{e}$. (a) and (b) Cases of varying ν. (c)–(d) Cases of varying Re. (Left) panels are from the straight path and (right) from the sinusoidal path. The black dashed lines delineate the borders between the meaningful and trivial solutions.

moving through the objective space. Considering the fact that the mapping between the objective and parameter space is neither necessarily smooth nor continuous, we emphasize that regions or even individuals in the Pareto optimal objective space must be 'classified' into different groups that needs to be treated separately. For our study there is an obvious choice for classification, swimmers versus non-swimmers. As noted previously, there are effectively trivial solutions when $\bar{E}$ is near zero and the error is correspondingly high. This occurs when the contraction strength is sufficiently small such that the soft swimmer barely moves. By excluding these high error individuals (above roughly half the maximum error), we are left with parameter regions that may exhibit qualitatively clear trends in the objective space.

Figure 9 shows the trends of $k_{p,position}$ versus error for all cases used in the optimization study at different values of ν and Re. When near the minimum error, $k_{p,position}$ appears to reach maximum values, which corresponds to the optimal solutions near the upper bound of contraction strength α_0. For fairly large error values, $k_{p,position}$ becomes negligible, corresponding to those trivial solutions with low $\bar{E}$. From the PID controller formulation in equation (9), $\alpha_0 \propto k_{p,position} e_1$, suggesting that when α_0 is properly bounded, larger controller gain $k_{p,position}$ results in reduced error.

Table 1. Summary of the variables and objectives considered in the optimization.

Variables	Objectives
$k_{p,position}$	$\bar{e}$
$k_{i,position}$	C_{ot}
$k_{d,position}$	$\bar{E}$
$k_{p,heading}$	
$k_{i,heading}$	
$k_{d,heading}$	

Besides the $k_{p,position} - Error$ relations, however, we did not find other clear trends when we sweep through the parameter space and connect the tuning parameters to the objectives. The data appear to be highly noisy, which is primarily due to the stochastic nature of evolutionary methods. We have observed that often times, they are able to converge rapidly to a certain optimum region, and then slowly approach the optimal solution(s) within via a stochastic search. Nevertheless, when comparing the obtained optimal tuning

parameters for different target path (i.e. straight versus sinusoidal) as well as across Reynolds numbers (e.g. see figure 9), we have found that their values all fall into approximately the same ranges, indicating that these solutions indeed characterize the global optima. In other words, the proposed optimization approach seems to have produced PID controllers with near-optimal behavior across varying target behaviors and fluid environments.

5. Conclusion

In this paper we presented a new computational framework for optimizing feedback control of soft robotic fish enabled by muscle-like actuation. A novel fictitious domain/active-strain method [30] was employed to handle the resultant fluid-structure interaction when local contractile active strains—emulating muscle actuation—are imposed on the soft swimmer. In particular, using a 2D elastic beam with finite width as a model for the soft swimmer, we demonstrated versatile swimming motions (forward swimming and turning at different velocities and radii, for example) by varying the strength and bias of the active strains imposed on both sides of the swimmer. Two PID controllers are adopted for adjusting the actuation strength (α_0) and bias (β), respectively, for the swimmer to track a moving target. With this setup, multi-objective optimization of the controller parameters was conducted using the U-NSGA-III algorithm, where three objectives were considered, including the tracking error, cost of transport, and elastic strain energy. The PID controller parameters were optimized using a series of moving target trajectories, involving different speeds and Reynolds numbers for two types of paths (straight and sinusoidal). By analyzing the resulting Pareto fronts, the study revealed the trends of how the obtained values of objectives are influenced by the target trajectory conditions. It also showed the correlation and trade-offs among the objectives under feedback control, as well as how the optimized controller parameters are related to the objectives and trajectory conditions. Overall, this work has shown the feasibility of using high-fidelity CFD to design and optimize feedback control for soft robotic fish subject to multiple, potentially conflicting objectives.

There are a few directions for future work. First, we will consider the extension of the presented framework to the case where the soft swimmer has a 3D geometry and a more general form of distributed actuation. However, compared to the 2D cases, dynamic instabilities can raise significant challenges in robots design and optimization, especially for light-weight structures moving in fluid or air [15, 37]. Hence large-scale computation is desirable to thoroughly explore the parameter space to identify the phase boundaries of the stable dynamic regime, which may further suggest simplified dynamic models for analysis. In the meantime, methods of sensitivity analysis can be included in the optimization process to uncover and compensate for these instabilities [2, 42]. Second, while PID controllers were used as an example of model-free controller in this work, we plan to exploit the computation data and system ID techniques to obtain the dynamic model of a soft swimmer, based on which model-based controllers (such as linear quadratic regulator (LQR) and model-predictive control [7]) will be developed and evaluated. Ultimately, it is our plan to experimentally validate the modeling, control, and optimization methods with a soft robotic fish prototype actuated by smart materials (e.g. shape memory alloys or dielectric elastomer actuators).

Acknowledgments

This work was supported in part by an MSU Strategic Partnership Grant 16-SPG-Full-3236 (AH, TG and XT) and an NSF Grant No. CBET-1702987 (TG).

ORCID iDs

Xiaobo Tan https://orcid.org/0000-0002-5542-6266
Tong Gao https://orcid.org/0000-0001-5049-8538

References

[1] Ambrosi D and Pezzuto S 2012 Active stress versus active strain in mechanobiology: constitutive issues *J. Elast.* **107** 199–212
[2] Avila S L, Lisboa A C, Krahenbuhl L, Carpes W P, Vasconcelos J A, Saldanha R R and Takahashi R H C 2006 Sensitivity analysis applied to decision making in multiobjective evolutionary optimization *IEEE Trans. Magn.* **42** 1103–6
[3] Bartlett N W, Tolley M T, Overvelde J T, Weaver J C, Mosadegh B, Bertoldi K, Whitesides G M and Wood R J 2015 A 3D-printed, functionally graded soft robot powered by combustion *Science* **349** 161–5
[4] Becker A, Masoud H, Newbolt J, Shelley M and Ristroph L 2015 Hydrodynamic schooling of flapping swimmers *Nat. Commun.* **6** 8514
[5] Belytschko T, Liu W K, Moran B and Elkhodary K 2013 *Nonlinear Finite Elements for Continua and Structures* (New York: Wiley)
[6] Bhalla A, Bale R, Griffith B and Patankar N 2013 A unified mathematical framework and an adaptive numerical method for fluidstructure interaction with rigid, deforming, and elastic bodies *J. Comput. Phys.* **250** 446–76
[7] Castano M and Tan X 2019 Model predictive control-based path following for tail-actuated robotic fish *J. Dyn. Syst. Meas. Control* **141** 071012
[8] Chester S and Anand L 2010 A coupled theory of fluid permeation and large deformations for elastomeric materials *J. Mech. Phys. Solids* **58** 1879–906
[9] Christianson C, Goldberg N N, Deheyn D D, Cai S and Tolley M T 2018 Translucent soft robots driven by frameless fluid electrode dielectric elastomer actuators *Sci. Robot.* **3** eaat1893
[10] Dai L, He G, Zhang X and Zhang X 2018 Stable formations of self-propelled fish-like swimmers induced by hydrodynamic interactions *J. R. Soc. Interface* **15** 20180490
[11] Deb K and Jain H 2014 An evolutionary many-objective optimization algorithm using reference-point-based nondominated sorting approach, part I: solving problems with box constraints *IEEE Trans. Evolutionary Comput.* **18** 577–601

[12] Deb K, Pratap A, Agarwal S and Meyarivan T 2002 A fast and elitist multiobjective genetic algorithm: Nsga-ii *IEEE Trans. Evolutionary Comput.* **6** 182–97
[13] Dombrowski T, Jones S, Katsikis G, Bhalla A, Griffith B and Klotsa D 2019 Transition in swimming direction in a model self-propelled inertial swimmer *Phys. Rev. Fluids* **4** 021101
[14] Drotman D, Jadhav S, Karimi M, Dezonia P and Tolley M T 2017 3D printed soft actuators for a legged robot capable of navigating unstructured terrain *IEEE Int. Conf. on Robotics and Automation* (ICRA) pp 5532–8
[15] Fang F, Ho K, Ristroph L and Shelley M 2017 A computational model of the flight dynamics and aerodynamics of a jellyfish-like flying machine *J. Fluid Mech.* **819** 621
[16] Fauci L and McDonald A 1995 Sperm motility in the presence of boundaries *Bull. Math. Biol.* **57** 670–99
[17] Gazzola M, Tchieu A A, Alexeev D, de Brauer A and Koumoutsakos P 2016 Learning to school in the presence of hydrodynamic interactions *J. Fluid Mech.* **789** 726–49
[18] Gazzola M, Van Rees W M and Koumoutsakos P 2012 C-start: optimal start of larval fish *J. Fluid Mech.* **698** 5–18
[19] Glowinski R, Pan T-W, Hesla T I and Joseph D D 1999 A distributed Lagrange multiplier/fictitious domain method for particulate flows *Int. J. Multiph. Flow* **25** 755–94
[20] Griffith B and Luo X 2017 Hybrid finite difference/finite element immersed boundary method *Int. J. Numer. Method Biomed. Eng.* **33** e2888
[21] Hamlet C, Fauci L J and Tytell E D 2015 The effect of intrinsic muscular nonlinearities on the energetics of locomotion in a computational model of an anguilliform swimmer *J. Theor. Biol.* **385** 119–29
[22] Hoover A, Griffith B and Miller L 2017 Quantifying performance in the medusan mechanospace with an actively swimming three-dimensional jellyfish model *J. Fluid Mech.* **813** 1112–55
[23] Katz Y, Tunstrøm K, Ioannou C C, Huepe C and Couzin I D 2011 Inferring the structure and dynamics of interactions in schooling fish *Proc. Natl Acad. Sci.* **108** 18720–5
[24] Kern S and Koumoutsakos P 2006 Simulations of optimized anguilliform swimming *J. Exp. Biol.* **209** 4841–57
[25] Lee E H 1969 Elastic-plastic deformation at finite strains *J. Appl. Mech.* **36** 1–6
[26] Lee E H and Liu D T 1967 Finite-strain elastic-plastic theory particularly for plane wave analysis *J. Appl. Phys.* **38** 19–27
[27] Li L, Sherwin S and Bearman P 2002 A moving frame of reference algorithm for fluid/structure interaction of rotating and translating bodies *Int. J. Numer. Methods Fluids* **38** 187–206
[28] Lighthill J 1975 *Mathematical Biofluid Dynamics* (Philadelphia, PA: SIAM)
[29] Lighthill M J 1960 Note on the swimming of slender fish *J. Fluid Mech.* **9** 305–17
[30] Lin Z, Hess A, Yu Z, Cai S and Gao T 2019 A fluid-structure interaction study of soft robotic swimmer using a fictitious domain/active-strain method *J. Comput. Phys.* **376** 1138–55
[31] Majidi C 2014 Soft robotics: a perspective-current trends and prospects for the future *Soft Robot.* **1** 5–11
[32] Miriyev A, Stack K and Lipson H 2017 Soft material for soft actuators *Nat. Commun.* **8** 596
[33] Nawroth J, Lee H, Feinberg A, Ripplinger C, McCain M, Grosberg A, Dabiri J and Parker K 2012 A tissue-engineered jellyfish with biomimetic propulsion *Nat. Biotechnol.* **30** 792–7
[34] Park S *et al* 2016 Phototactic guidance of a tissue-engineered soft-robotic ray *Science* **353** 158–62
[35] Parrish J K, Viscido S V and Grunbaum D 2002 Self-organized fish schools: an examination of emergent properties *Biol. Bull.* **202** 296–305
[36] Peskin C S 2002 The immersed boundary method *Acta Numer.* **10** 479–517
[37] Ristroph L and Childress S 2014 Stable hovering of a jellyfish-like flying machine *J. R. Soc. Interface* **11** 20130992
[38] Rivera D E, Morari M and Skogestad S 1986 Internal model control: PID controller design *Ind. Eng. Chem. Process Des. Dev.* **25** 252–65
[39] Rus D and Tolley M T 2015 Design, fabrication and control of soft robots *Nature* **521** 467–75
[40] Seada H and Deb K 2016 A unified evolutionary optimization procedure for single, multiple, and many objectives *IEEE Trans. Evolutionary Comput.* **20** 358
[41] Suo Z 2010 Theory of dielectric elastomers *Acta Mech. Solida Sin.* **23** 549–78
[42] Tanino T 1988 Sensitivity analysis in multiobjective optimization *J. Optim. Theory Appl.* **56** 479–99
[43] Teran J, Fauci L and Shelley M 2010 Viscoelastic fluid response can increase the speed and efficiency of a free swimmer *Phys. Rev. Lett.* **104** 038101
[44] Tian H, Wang Z, Chen Y, Shao J, Gao T and Cai S 2018 Polydopamine-coated main-chain liquid crystal elastomer as optically driven artificial muscle *ACS Appl. Mater. Interfaces* **10** 8307–16
[45] Tytell E D, Leftwich M C, Hsu C-Y, Griffith B E, Cohen A H, Smits A J, Hamlet C and Fauci L J 2016 Role of body stiffness in undulatory swimming: insights from robotic and computational models *Phys. Rev. Fluids* **1** 073202
[46] van Rees W M, Gazzola M and Koumoutsakos P 2015 Optimal morphokinematics for undulatory swimmers at intermediate Reynolds numbers *J. Fluid Mech.* **775** 178–88
[47] Yu Z 2005 A DLM/FD method for fluid/flexible-body interactions *J. Comput. Phys.* **207** 1–27